Measurement of Liquid Water Accumulation in a PEMFC with Dead-Ended Anode

Jason B. Siegel,[a,*,z] **Denise A. McKay,**[a,**] **Anna G. Stefanopoulou,**[a]
Daniel S. Hussey,[b,*] **and David L. Jacobson**[b]

[a]*University of Michigan, Ann Arbor, Michigan 48109, USA*
[b]*National Institute for Standards and Technology, Gaithersburg, Maryland 20899, USA*

The operation and accumulation of liquid water within the cell structure of a polymer electrolyte membrane fuel cell (PEMFC) with a dead-ended anode is observed using neutron imaging. The measurements are performed on a single cell with 53 cm^2 active area, Nafion 111-IP membrane, and carbon cloth gas diffusion layer. Even though dry hydrogen is supplied to the anode via pressure regulation, accumulation of liquid water in the anode gas distribution channels was observed in most tested conditions. Moreover, the accumulation of liquid water in the anode channels is followed by a significant voltage drop. Anode purges and cathode surges are also used as a diagnostic tool for differentiating between anode and cathode water flooding. The rate of accumulation of liquid water, and its impact on the rate of cell voltage drop is shown for a range of temperature, current density, cathode inlet RH, and air stoichiometric conditions. Operating the fuel cell under dead-ended anode conditions offers the opportunity to observe water dynamics and measured cell voltage during large and repeatable transients.
© 2008 The Electrochemical Society. [DOI: 10.1149/1.2976356] All rights reserved.

The electrochemical power generation of a popular category of fuel cells depends on the proton-conducting properties of their polymer electrolyte membranes. The ability of the membrane to conduct protons increases with increasing water content. However, polymer electrolyte membrane fuel cells (PEMFCs) operate below the boiling point of water, causing excess water to condense and restrict gas delivery or block the catalyst active area. The buildup of water mass, referred to as flooding, in an operating fuel cell was first observed with neutron imaging in Ref. 1. The impact of this flooding phenomena is a recoverable reduction in the power output of the fuel cell, seen by a decrease in cell voltage,[2,3] but can also lead to irrecoverable material degradation.[4,5]

This paper presents the neutron imaging of liquid water accumulation in a PEMFC operating with a dead-ended anode. Modeling and testing for anode flooding conditions is rare because most experimental fuel cells operate under flow-through conditions for which anode flooding is highly unlikely. Here a solenoid valve placed downstream from the cell allows for an occasional purging event with high hydrogen flow rate to remove water from the anode, preventing severe voltage drop and reactant starvation. Optimal scheduling of purge events is necessary to prolong fuel cell life and minimize wasted hydrogen. An adjustable purging schedule applied to a stack with a dead-ended anode can enable high hydrogen utilization and remove the need for costly, heavy, and bulky anode humidification and recirculation hardware. Furthermore, understanding the water removal with anode purging is important for designing shutdown procedures to alleviate damage caused by freeze and thaw cycling.

Therefore models which accurately predict the accumulation and removal of water are necessary. If in addition to water accumulation the model can also predict the resulting cell voltage, it could be used in combination with voltage measurement to allow real-time adaptation of the purging events in response to component aging, environmental changes, and system faults. Specifically, the estimated voltage is compared with the actual voltage, and the error is used to adjust the model-based purge schedule. A similar model-based technique was used for the estimation of hydrogen starvation[6] and control of the hydrogen production rate from a fuel processor.[7] Hence, the experiments and experimental results detailed here sought to confirm that a consistent correlation between water accumulation and voltage degradation exists.

To this end, our experimental results offer the opportunity to observe water dynamics and measured cell voltage during large and repeatable transients and hence provide useful data for calibrating and validating simple lumped parameter transient models[8,9] during anode flooding conditions. Despite some limitations of the imaging system,[10] with careful cell design and masking the approximate location of the liquid water within the cell structure can be inferred, similar to the work of Ref. 2, 3, and 11-16. Neutron imaging experiments with higher resolution in the membrane through-plane direction could provide more information on the intrinsic mechanism of voltage degradation during anode flooding. However, higher spatial resolution imaging requires longer exposure times[17] and hence, the method is impractical for calibrating or validating transient models with a time resolution less than 1 min. In our setup, we distinguish anode vs cathode channel flooding using controlled cathode surging and anode purging events. During an anode purge, fed with dry hydrogen, a high gas flow rate through the cell is used to remove the liquid water stored in the anode. During a cathode surge the air flow is momentarily and abruptly increased beyond the nominal excess ratio to remove any liquid water stored in the cathode.

It is demonstrated that liquid water accumulates in the anode gas channels, and this buildup of liquid water is well correlated with the dynamic cell voltage response during the majority of the experiments, as originally predicted in Ref. 18. This data also indicates that there is sometimes significant voltage drop, even if the mass of water does not increase in the fuel cell. Hence, water flooding cannot be considered always responsible for the voltage drop and nitrogen accumulation in the anode should also be considered.[19,20] Our conclusions about channel water mass are based on several homogeneity assumptions which ignore the difference in the stored liquid water mass in the gas diffusion layer (GDL) under the channels as compared to areas under lands.[10,21] Nevertheless, the data and data analysis provide useful new information regarding PEMFC transient behavior.

Experimental

Experiments were conducted at the Neutron Imaging Facility at the National Institute for Standards and Technology (NIST) Center for Neutron Research.[17] We used the amorphous silicon detector for its 1 Hz image acquisition rate to capture the change in mass of liquid water over time. A 1 cm diameter aperture was used for the experiment, with a neutron fluence rate I_0 of 7.2×10^6 cm^{-2} s^{-1} and a neutron flight path of 6 m. In this case, the ratio of source-to-detector distance over the source aperture diameter (L/D) was equal to 600. The width of a pixel in the image corresponds to 127 μm, but the resolution of the imaging system is about 250 μm as a result of scintillator blooming.[17]

* Electrochemical Society Active Member.
** Electrochemical Society Student Member.
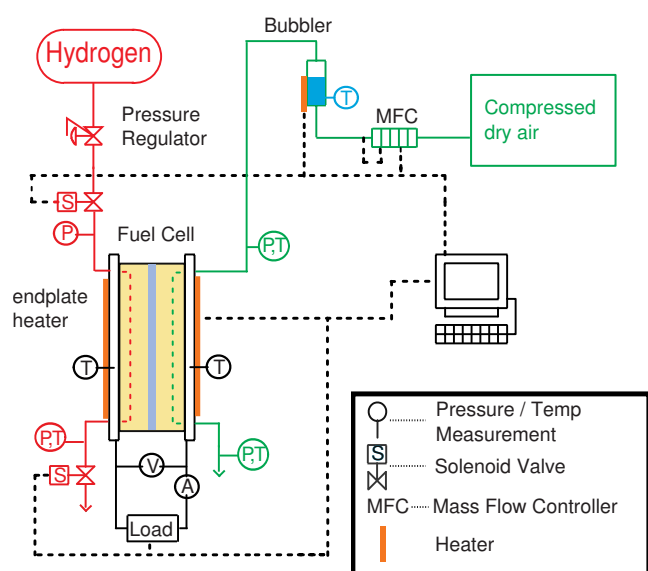z E-mail: siegeljb@umich.edu

Figure 1. (Color online) Experimental hardware detailing sensor and actuator locations.

Figure 2. (Color online) Neutron images of the fuel cell active area before and after anode purge events, indicating the actual cell orientation. The cell was operated at 566 mA cm^{-2}, 55°C, with fully humidified air at a stoichiometry of 200% for cathode and dry hydrogen supplied to anode.

The NIST test stand is used to supply a humidified gas stream to the cathode in flow-through operation. The air is humidified using a bubbler, and it is assumed that the gas leaving the bubbler is saturated at the water temperature. The inlet relative humidity (RH) can be calculated at the fuel cell temperature by assuming the air has a dewpoint temperature equal to the bubbler temperature. A portable anode purging system was constructed, which allows dead-ended operation of the fuel cell. This anode purge system consists of a pressure regulator, which supplies dry hydrogen to the anode inlet, and a solenoid valve downstream of the anode outlet. A needle valve placed downstream from the solenoid valve is used to set the desired flow rate during an anode purge event. The pressure drop across the needle valve is used to reduce the gas flow rate leaving the channel during an anode purge event. This valve was adjusted prior to beginning and kept fixed for the duration of the experiments. The anode gas flow rate during a purge is about 5 slpm. Between purges the anode is supplied with dry hydrogen via pressure regulation, which provides a dry hydrogen flow at a stoichiometry equal to one, as shown in Fig. 1. Voltage, current, pressure, temperature, and cathode flow rate measurements were recorded continuously at 1 Hz resolution. The image data was selectively recorded when repeatable large transients were observed. Due to the large file size it was not desirable to capture data for all times, creating gaps in the measured liquid water mass data.

The cell was comprised of a single 53 cm^2 Nafion 111-IP membrane[c] which is 25.4 μm thick with anode and cathode catalyst layers containing a Pt areal density of 0.3 mg cm^{-2} purchased from Ion Power. SGL 10BB nonwoven carbon GDLs were used, which have an uncompressed thickness of 420 μm and a porosity of ε = 0.84. The cell hardware, purchased from Electrochem, consisted of aluminum endplates, gold-coated aluminum current collectors, and resin-impregnated graphite flow fields. Resin-impregnated graphite is used to prevent liquid water from accumulating inside the pore structure of the graphite.[22] The graphite plates were thinned to 0.32 cm to reduce neutron attenuation. The anode gas channels are straight with a channel width of 2.08 mm, depth of 1.78 mm, and

land width of 0.838 mm. A semiserpentine flow path is used on the cathode with five parallel paths, each having a channel width of 0.686 mm, a channel depth of 0.991 mm, and a land width of 0.762 mm. A square 45 W resistive heater, with a surface area of 58 cm^2, was attached to each end plate to ensure uniform heating and maintain the desired temperature at low current density.

Quantification of Liquid Water Mass

The attenuation properties of a neutron beam passing through an object can be used to form a projected image on a detector, similar to X-ray radiography. Neutrons are strongly scattered by hydrogen atoms and only weakly interact with the other materials used in PEMFCs, such as aluminum and carbon. The scattering interaction is also density dependent; therefore, neutron imaging is particularly useful for measuring liquid water present in the cell due to the high density of hydrogen atoms in liquid water but is unable to detect hydrogen gas or water vapor. This technique provides a useful tool for in situ measurement of liquid water content while employing commercial fuel cell materials with realistic cell designs. The use of these materials reduces the possibility of temperature gradients induced by selection of nonstandard materials, which would otherwise greatly impact the formation of liquid water within the cell.

Figure 2 shows two images collected before and after a purge event. The areas with high liquid water accumulation are clearly visible in the top left frame, which corresponds to a condition before an anode purge event. The second frame in Fig. 2 shows the drier neutron image collected after the purge. The downward pointing vector **g** indicates the direction of gravity.

The image, $I(j,k)$, formed by scattering and absorption of neutrons can be modeled by the Beer–Lambert law

$$I(j,k) = I_0(j,k)\exp\left[-\sum_{l=1}^{N} \mu_l t_l(j,k) \right] \quad [1]$$

where $I_0(j,k)$ is the incident flux rate of neutrons, N is the number of material layers in the object, t_l is the thickness of each layer, and μ_l is the linear attenuation coefficient of each layer.

In order to quantify the thickness of liquid water, we must determine the amount of attenuation which is caused by water in the image. A section of the image outside the active area, defined by S_P,

[c] Certain trade names and company products are mentioned in the text or identified in an illustration in order to adequately specify the experimental procedure and equipment used. In no case does such identification imply recommendation or endorsement by the National Institute of Standards and Technology, nor does it imply that the products are necessarily the best available for the purpose.
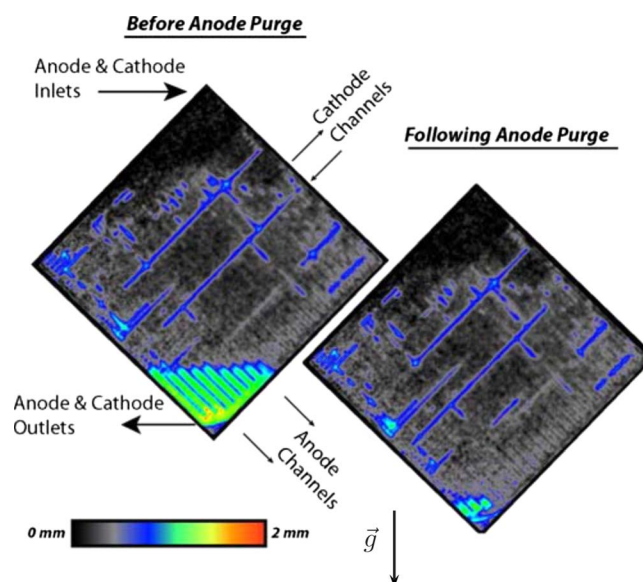
is used to normalize each image before processing to account for fluctuations in the nuclear reactor power output and $I_0(j,k)$ over time, according to

$$I^{norm}(j,k) = \frac{I(j,k)}{\Sigma_{j,k \in S_P} I(j,k)} \qquad [2]$$

To reduce systematic error, care was taken to ensure reference images, $I_{dry}^{norm}(j,k)$, were taken of a completely dry cell, and 1500 images were averaged to reduce noise in the image. In order to account for the effects of thermal expansion, which cause portions of the cell to move within the imaging frame, dry reference images were taken at 5°C increments over the operating temperature range of the fuel cell. The relative neutron transmission, found by dividing an image by the dry reference image of the cell, can be used to calculate water thickness, assuming that the attenuation caused by everything but liquid water remains unchanged since the reference image was captured. A 3 × 3 median filter is applied to the images to further reduce random noise before calculating the liquid water thickness. The thickness of the water layer was calculated using

$$t_w(j,k) = -\frac{1}{\mu_w} \ln \left[\frac{I^{norm}(j,k)}{I_{dry}^{norm}(j,k)} \right] \qquad [3]$$

and the experimentally obtained attenuation coefficient μ_w = 0.3708 ± 0.0008 mm^{-1},[17] which is valid for liquid water thickness less than 1 mm.

Liquid water quantification is further complicated by instrument broadening caused by the scintillator screen, scattering of neutrons by objects in the beam, and detector noise.[11,23] The trends in the data will still be evident without correction for these effects. Quantification of the error introduced by each phenomena is currently under investigation at NIST.[17]

Temporal averaging to reduce uncertainty.— The measured uncertainty in water volume for a single pixel in the detector system sampled at the 1 Hz rate is 0.32×10^{-6} cm^3 using (L/D) = 450,[17] which is different from our setup (L/D) = 600. The measured uncertainty can be scaled to account for the different neutron flux used in the experiment by multiplying by the ratio of the square root of the fluence rates, which yields a per pixel liquid water volumetric uncertainty of 0.537×10^{-6} cm^3. This relationship can be derived from the equation for the theoretical uncertainty[17]

$$\delta_t = \frac{1}{\mu} \sqrt{\frac{1 + e^{\mu t}}{I_o A T \eta}} \approx \frac{1}{\mu} \sqrt{\frac{2}{I_o A T \eta}} \qquad [4]$$

where t is the water thickness, μ is the attenuation coefficient, I_o is the fluence rate, A is the area, T is the integration time, and η is the detector efficiency. Equation 4 also indicates that a reduction in uncertainty of the measured liquid water volume can be achieved at the expense of temporal resolution by averaging several frames. The uncertainty in an averaged frame of 11 s as compared to 1 s is decreased by a factor of $\sqrt{1/T} \approx 0.3$. Because the time constant associated with liquid water accumulation in the GDL is on the order of 100 s,[22,24] the 11 s imaging rate was used. The resulting liquid water volume uncertainty is 0.16×10^{-6} cm^3 pixel^{-1}, which corresponds to a water thickness of 10 μm. Unfortunately, the temporal averaging we performed exacerbates the difficulty in tracking movement of water droplets and slugs in the channels. Liquid water droplet movement with the gas stream in the channel could be much faster than the 1 s imaging time, and therefore during a cathode surge or anode purge liquid water flow in the channel would appear blurred, even without averaging at the fastest exposure rate of the imaging system.

Masking.— The processed water thickness image, $t_w(j,k)$, is a two-dimensional (2D) projection of the liquid water inside the fuel cell. In order to infer the location of liquid water in the third dimension, a knowledge of the physical material structure can be combined with logical arguments. For example, liquid water cannot be
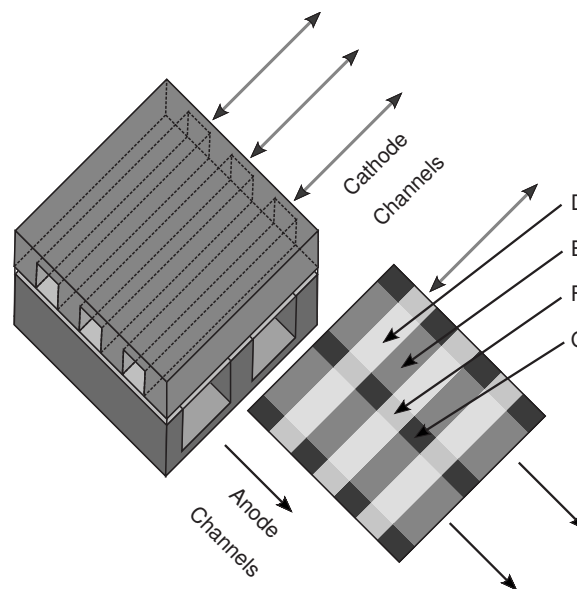

Figure 3. Schematic of fuel cell layers. The beam direction is into the page and perpendicular to the membrane.

located within an impervious solid material. Several masking techniques have been used to analyze neutron images.[2,3,13,14] We employ a similar process to estimate the mass of liquid water in three layers: the anode channel, cathode channel, and combined membrane (MB) and GDL layer (GDLMB, which consists of both anode and cathode GDLs). The masks are formed using the drawings of the graphite plates. Mask A defines the active area of the fuel cell, mask B is for the anode channels, and mask C is for the cathode channels. Four mutually disjoint masks, D–G, identify regions of the fuel cell corresponding to the different possible combinations of channels and lands on each side of the membrane as shown in Fig. 3. The area of each mask and their logical relationships are shown in Table I. The water thickness in the combined membrane and GDL layer can be directly measured from the images for regions identified by mask G, which contain both anode and cathode lands and therefore water could not be present in either of the other two layers.

Local spatial averaging.— Estimation of the distribution of liquid water in the third dimension using masking over the entire active area requires consideration of the significant spatial variations in the liquid water thickness along the channels. Therefore, a local 2D spatial average is constructed. Specifically, the active area is partitioned into a 9 × 9 grid of 81 segments similar to Ref. 3. A 9 × 9 grid is chosen corresponding to the nine segments of parallel cathode channels as seen in Fig. 4, which is overlaid on mask C. Within each of the 81 segments, the flow of reactant gases is in the same direction. Due to a manufacturing error the cathode inlet and outlet manifolds were incorrectly positioned, rendering the first and last serpentine flow pass ineffective. The cathode inlet should be

Table I. Masks.

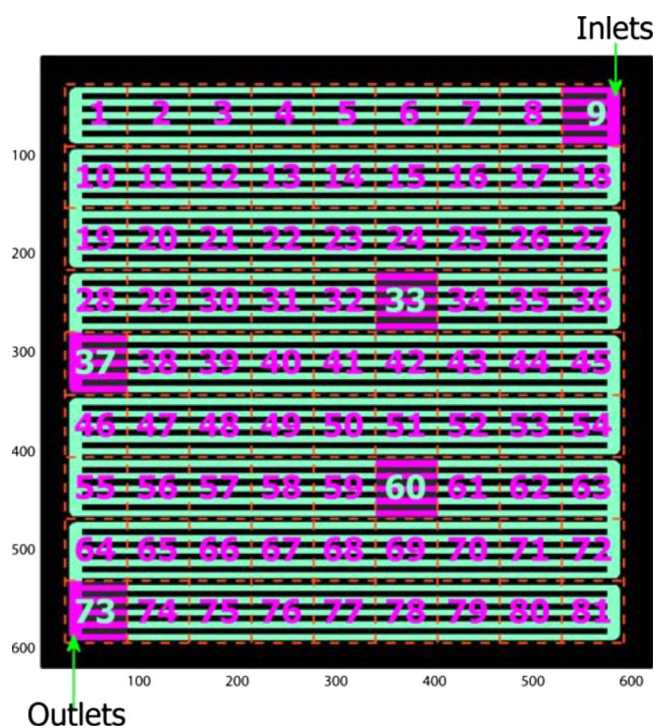| Mask	Description	No. pixels	Relationship
A	Active area	313,600	$D \cup E \cup F \cup G$
B	Anode channel area	234,099	
C	Cathode channel area	169,392	
D	Both Ch + MB + GDL	128,047	$B \cap C$
E	An Ch + MB + GDL	106,052	$(B \cap \bar{C}) \cap A$
F	Ca Ch + MB + GDL	41,345	$(\bar{B} \cap C) \cap A$
G	MB + GDL only	38,155	$(\bar{B} \cap \bar{C}) \cap A$
H	Subset of G	11,239	$H \subset G$

Figure 4. (Color online) The cathode channel, mask C, is partitioned into 81 segments for the evaluation of the spatial distribution in cathode channel liquid water. Five representative segments are highlighted and shown in later analysis.

Figure 5. (Color online) Measured average liquid water thickness in the combined membrane/GDL layer for the entire active area (top subplot) and within selected segments (subsequent subplots) from the same data set shown in Fig. 6.

located in segment 1, for proper operation, but is instead located in segment 9 as shown in Fig. 4. As a result, segments 1–8 and 74–81 are not included in the flow path; therefore, no excess air is passed through these segments of the cathode during operation of the cell. Hence, the cathode channel exhibits an unusual accumulation of liquid water in these segments. Due to the orientation of the cell, prior to masking, each thickness image is rotated 44.3° to the right using a bicubic interpolation method to facilitate registration with the mask. In the rotated orientation, studies can be performed along the channels by traversing the coordinate axis of the image. Note that segment 9, which is highlighted in Fig. 4, corresponds to the upper corner of the fuel cell shown in Fig. 2. Segment 9 is also the location of the gas inlets where the dry hydrogen and humidified air enter the anode and cathode channels, respectively.

The fuel cell conditions are assumed to be uniform within each of the 81 segments. Five image masks (D–H) are applied to each of the 81 segments individually, and the average liquid water thickness in each of the masked regions is calculated for each segment. A fifth mask H, which is a subset of the points in mask G which are not adjacent to either channel, is used to get a more accurate estimate of the water content in the combined GDL and membrane layer. This mask reduces the effects of instrument broadening and neutron scattering when there is liquid water present in the neighboring channels.[11,17] Since only points near the center of the lands are counted, the effect of different gas flow distributions in the GDL in the adjacent regions, underneath the channel as compared to the land, on liquid accumulation may not be accurately represented.

The top subplot in Fig. 5 shows a comparison of the average water thickness calculated using masks G and H over the entire active area for the combined membrane and GDL layer. When considering the entire active area, there is little difference between the average water thicknesses when using mask G as compared using mask H. However, for individual segments, a more significant difference between the applications of mask G vs mask H is observed, as indicated in the remaining subplots. The largest difference in average thicknesses is found in segment 73, located at the gas outlet
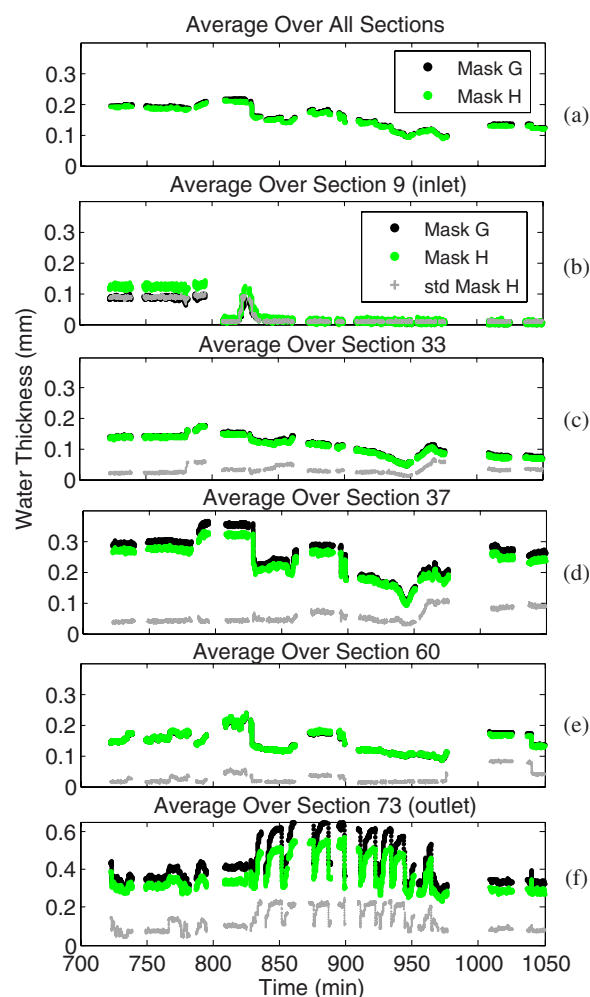
near the bottom of the cell. Due to the orientation of the cell and dead-ended anode, liquid water accumulates in this corner of the anode channel because it is forced by the reactant gas flow and gravity. A detailed description of the experimental testing conditions for this experiment can be found in Fig. 6.

The standard deviation in water thickness for points identified by mask G, shown in Fig. 5, provides a metric for how uniform the water content in the combined membrane and GDL layer is over that segment. A large standard deviation in thickness may indicate non-uniform conditions in the membrane and/or GDL. Scintillator blurring and/or scattering when a significant amount of water is present in the channel reduces the measured standard deviation but creates a systematic uncertainty. In the limiting case, when the water thickness is uniform, the standard deviation in measured thickness should be equal to that of the Poisson counting process given by Eq. 4, which increases with increasing water thickness. The large standard deviation measured for segment 9 between $t = 725$ and 800 min, shown in Fig. 5b, is likely due to condensation and buildup of liquid water near the cathode inlet manifold. A cathode surge conducted at around $t = 780$ min pushes liquid water out of segment 9, reducing the measured standard deviation in that segment. Segment 73 consistently contained the most water and therefore also has the highest standard deviation.

Channel liquid mass.— To calculate the mass of liquid water in the gas channels, assume that the water thickness in the combined
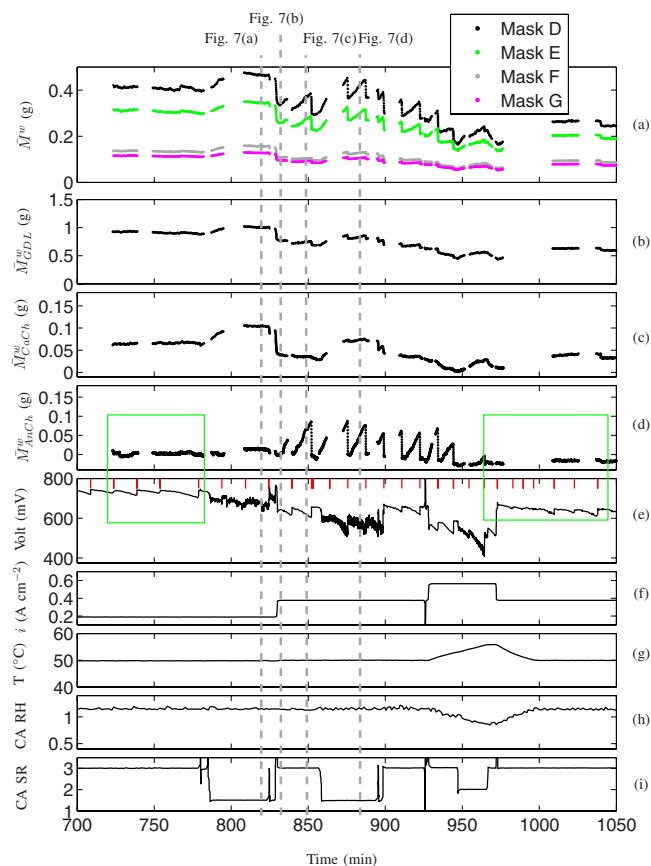
Figure 6. (Color online) Data set 1: Measured total liquid water mass, estimated GDL+MB and channel liquid water masses, voltage, current density, temperature, CA RH, and CA SR; fully humidified cathode gas (air) and dry hydrogen inlet. The (red) vertical lines in the voltage subplot indicate anode purges.

Table II. Cell operating conditions.

Parameter	Operating range
Anode inlet RH	0%
Cathode inlet RH	40–100%
Anode pressure	123.6 kPa absolute
Cathode pressure	120–125 kPa absolute
Cell temperature	40, 50, and 60°C
Cell current	0–30 A
Cell current density	0–566 mA cm^{-2}

Eq. 3. The results of this image processing and data analysis are shown in Fig. 6.

Three-dimensional computational models have demonstrated the possibility of a nonuniform liquid water distribution inside the GDL, with a buildup of water in regions underneath channel lands.[10,21] If the true water distribution in the GDL is concentrated under the lands, then the previous assumptions would lead to an underestimation of the amount of liquid water in the channel, and an overestimation of the GDL water content. Therefore this data analysis method represents a lower bound on the mass of accumulated water in the channels and an upper bound on the mass of water in the GDL.

Local averaging combined with masking yields more accurate results than simply averaging the masked regions over the entire active area due to the nonuniform distribution of water within the cell. The percent difference between the total liquid water mass and the estimated mass calculated via masked local averages, $\bar{M}^W_{AnCh}$ + $\bar{M}^W_{CaCh}$ + $\bar{M}^W_{GDLMB}$, is less than 2%, indicating that the relative uncertainty introduced by the assumption of a uniform water thickness in the combined membrane and GDL layer for each segment is small. Therefore we have a high level of confidence using the locally averaged and masked data to infer the mass of liquid water in each of the three layers: anode channel, cathode channel, and combined membrane GDL.

Results and Discussion

The neutron-imaging data were collected over 4 continuous days of testing (42 h) for the range of operating conditions summarized in Table II and shown in Fig. 6-10. The same cell was used throughout all the experiments, with pressure regulated dry hydrogen feed at various current densities, air stoichiometric ratios, cathode inlet RHs, and cell temperatures. It was assumed that the air supplied to the cathode had a dewpoint equal to the bubbler temperature. Control of the fuel cell endplate temperature and cathode bubbler temperature can therefore be used to achieve the desired cathode inlet RH. Relatively low current densities were used as compared to those typically reported in the literature. These low-to-medium current density conditions are interesting in portable and mobile applications where the system typically idles for a significant time. They are also conditions for which anode flooding is most predominant. However, at higher current density electro-osmotic drag tends to dry out the anode.[25]

One can notice that our operating temperature is also lower than PEMFCs are intended for, but this range was not intentional. Due to the software temperature calibration, the intended operating conditions were not attained and the cell was operated at a temperature colder than desired. The thermocouple was recalibrated after the experiment, and the corrected temperature is presented in the data. Because the bubbler temperature was higher than the fuel cell temperature for some of the experiments, in this case the dewpoint of the air entering the cathode channel was higher than the cell temperature, which is indicated by a calculated RH greater than 1, as shown in Fig. 6.

In the two subsections below we first present the results of the neutron image processing and demonstrate how the effects of the anode purge and surge events on the measured voltage can be used
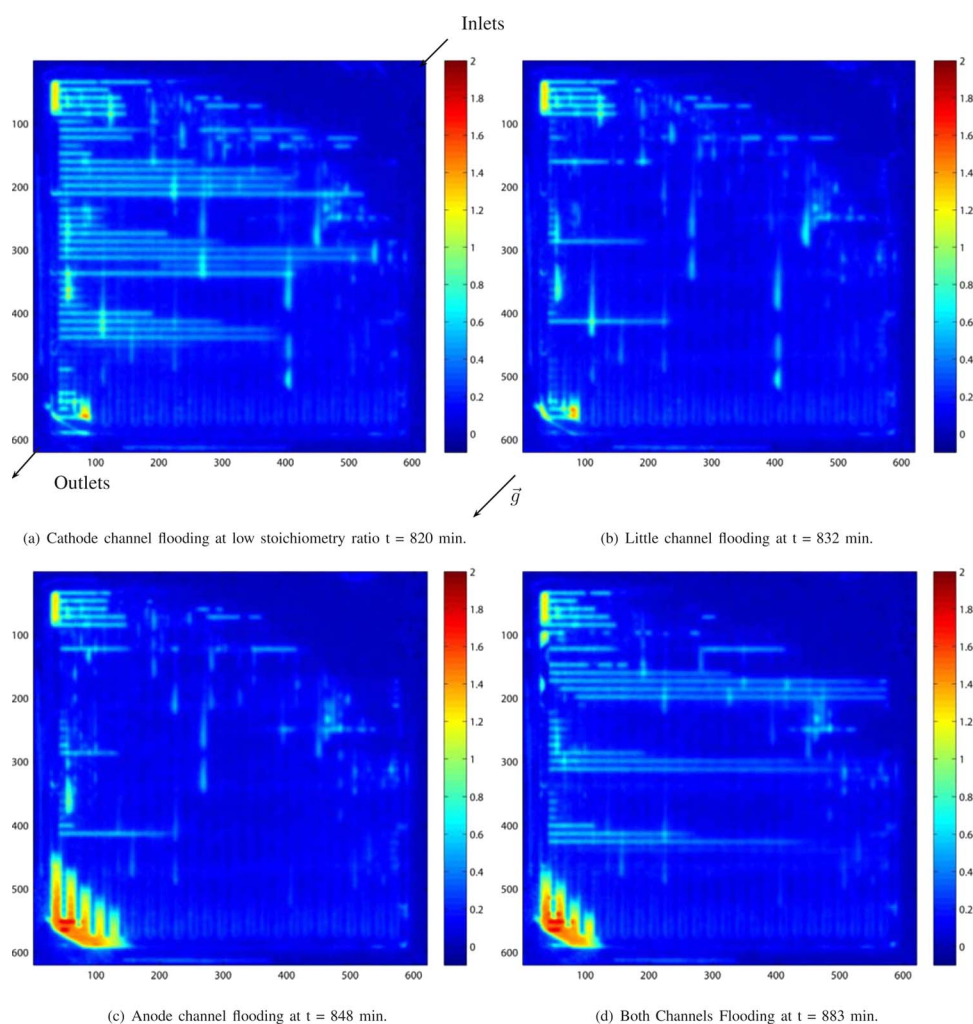
membrane and GDL layers is uniform over a segment, and then it is equal to the averaged thickness in the region defined by mask H. In this case the average liquid water thickness in the anode channel can be estimated by taking the difference between averaged water thickness in masked regions H (GDLMB) and E (GDLMB + AnCh) for each segment. Similarly, the average cathode channel liquid water thickness can be estimated by the difference between averaged water thickness in regions H and F. The total estimated liquid water mass in each layer of the cell is found by summing the masses calculated for each of the 81 segments, according to

$$\bar{M}^W_{GDLMB} = \rho_l A_P \sum_{i=1}^{81} N_{P,AA}[i] H[i] \qquad [5]$$

$$\bar{M}^W_{AnCh} = \rho_l A_P \sum_{i=1}^{81} N_{P,AnCh}[i](E[i] - H[i]) \qquad [6]$$

$$\bar{M}^W_{CaCh} = \rho_l A_P \sum_{i=1}^{81} N_{P,CaCh}[i](F[i] - H[i]) \qquad [7]$$

where ρ_l is the density of water, A_P is the area of the fuel cell corresponding to a single pixel in the detector, $N_{P,AA}[i]$, $N_{P,AnCh}[i]$, and $N_{P,CaCh}[i]$ are the number of pixels defining the active area, anode channel, and cathode channel, respectively, and $H[i]$, $E[i]$, and $F[i]$ are the measured average water thickness in segment i for each of the corresponding masks, where the thickness is given by

Figure 7. (Color online) Processed neutron images showing liquid water thickness (mm) under a variety of conditions.

(a) Cathode channel flooding at low stoichiometry ratio t = 820 min.

(b) Little channel flooding at t = 832 min.

(c) Anode channel flooding at t = 848 min.

(d) Both Channels Flooding at t = 883 min.

as a diagnostic tool to distinguish between operation with anode channel water flooding (anode plugging) or cathode channel water flooding (cathode plugging) conditions. Snapshots of the liquid water thickness images are shown to verify the purging and surging diagnostic capability. These snapshots also clarify differences in the 2D flow pattern, which affects the quality or ability of the purge event to remove water accumulated in the anode channels. Finally, we point to portions of the data where the water visualization indicates no anode plugging, however, repeatable voltage improvement is seen after every purge. These data sets indicate that there is (*i*) an anode nitrogen plugging problem and (*ii*) a GDL water mass value below which there is no liquid water flux to the anode channels and hence, anode water plugging is avoided. This information can be used to tune a value for the immobile saturation of liquid water inside the GDL, which is used in later sections to calibrate a simple model.

Channel water plugging.— Figure 6 shows the data from one of our full days of testing (6 h continuous operation), and Fig. 8-10 shows the rest of the data collected on three other days. A detailed discussion of the data shown in Fig. 6 is presented first. This data illustrates how changing the operating conditions can drive the system from a state of cathode channel flooding to anode channel flooding at low-to-medium current density. The first subplot of Fig. 6a shows the mass of liquid water in each of the four mutually disjoint masked regions, described previously, over the entire active area. The next three subplots show the estimated liquid water mass in each of the three layers (anode channel, cathode channel, and the combined membrane/GDL layer). The last four subplots of this fig-

ure display the important operating conditions which are typical model inputs:[8] current density (A cm^{-2}), end plate cell temperature (°C), cathode inlet RH, and cathode stoichiometric ratio.

The cell is initially operated at low current density (Fig. 6f) and high cathode stoichiometric ratio (CA SR) (Fig. 6i), and heaters are used to maintain the endplate temperature at 50°C (Fig. 6g). Figure 6h shows the estimated cathode inlet RH (CA RH) which is the ratio of the saturation pressure at the bubbler temperature over that of the cell temperature. At $t = 783$ min the cathode stoichiometry is decreased and water begins to accumulate in the cell, as seen in Fig. 6b and c. Cathode channel flooding is evident in the neutron radiographs, which can be seen in Fig. 7a at $t = 820$ min, and can be inferred by the rapid but small voltage fluctuations. This fluctuation in voltage occurs as the cathode channels are intermittently plugged with water, and the voltage is insensitive to the anode purges indicating the absence of anode plugging. We use the terms flooding and plugging to differentiate between the accumulation of water mass in the GDL and channel. Water accumulating in the channels forms slugs which block the flow of reactants along the channel; hence, the adoption of the term plugging.

Figure 7a also shows the buildup of liquid water after the 180° bends in the cathode semiserpentine flow path as observed in Ref. 26. However, the water in the cathode channel only accumulated after the 180° bends on the left side of the image, which corresponds to the "downhill" turnarounds when viewed in the original orientation as shown in Fig. 2. The gravity vector, **g**, delineates the image rotation relative to the cell orientation. The orientation of the cell and the effects of gravity may have a non-negligible effect on the
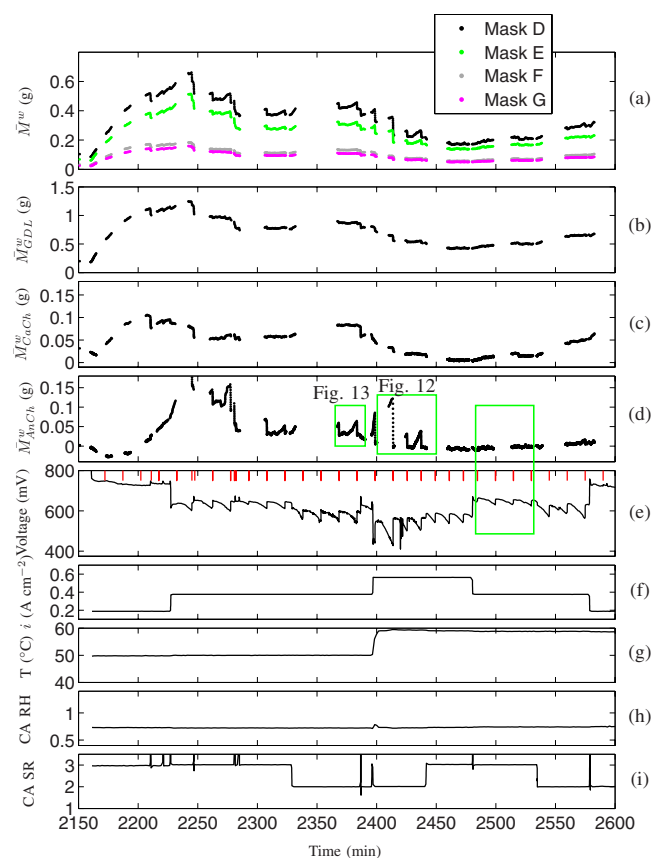
Figure 8. (Color online) Data set 2: Measured total liquid water mass, estimated membrane/GDL and channel liquid water masses, voltage, current density, temperature, CA RH, and CA SR. Subsaturated cathode gas (air) and dry hydrogen inlet. The (red) vertical lines in the voltage subplot indicate anode purges.
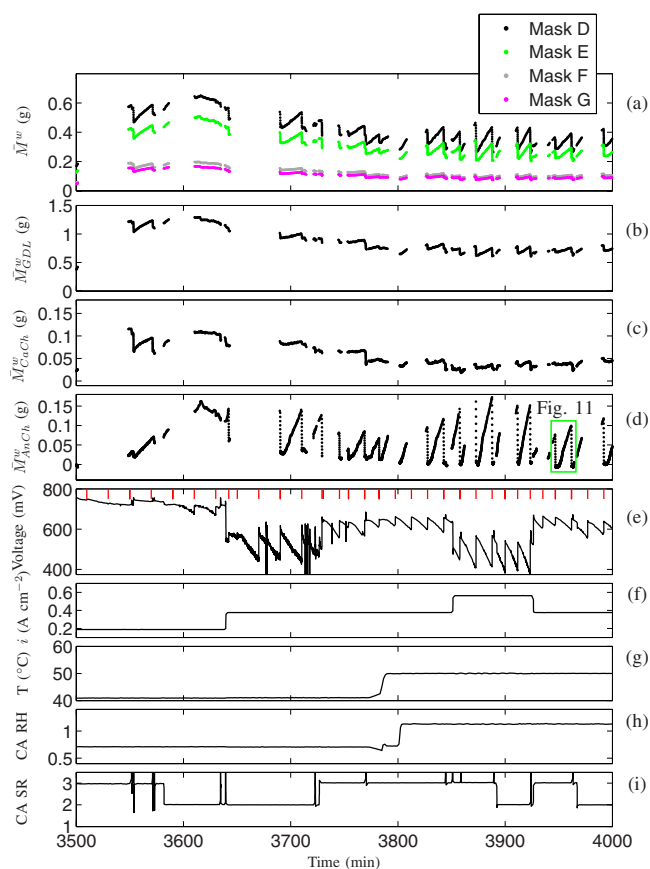

Figure 9. (Color online) Data set 3: Measured total liquid water mass, estimated membrane/GDL and channel liquid water masses, voltage, current density, temperature, CA RH, and CA SR. Subsaturated cathode gas (air), switching to fully humidified at $t = 3800$ min and dry hydrogen inlet. The (red) vertical lines in the voltage subplot indicate anode purges.

location of liquid water buildup within the channels.[27] This is different from common modeling assumptions of transport in the GDL, where gravitational effects are negligible.[28]

Just before $t = 825$ min the cathode is surged, removing liquid water from the cathode channels, and a sustained voltage recovery of 25 mV is observed. Following the surge, the current density and stoichiometry are both increased. The higher cathode gas velocity more readily removes liquid water from the cathode channel, as seen in Fig. 7b at $t = 832$ min. This new operating condition eventually leads to anode channel flooding, shown in Fig. 7c and clearly detected by the large periodic voltage increase following every purge. At $t = 858$ min the cathode stoichiometry is again decreased, leading to a condition in which both anode and cathode channel flooding occurs, as seen in Fig. 7d and detected by the small voltage fluctuations superimposed by purge-induced voltage improvements.

Data at lower cathode inlet RH (70%) also resulted in anode channel flooding, shown in Fig. 9 near $t = 3700$ min. A good example of cathode channel flooding can be seen shortly after startup in Fig. 8 at $t = 2215$ min, where a 25 mV sustained voltage recovery occurs following a cathode surge. Cathode flooding is also present at $t = 3554$ min in Fig. 9, under similar conditions of low cathode inlet RH and low current density 189 mA cm^{-2}. At the two higher current densities which were tested, cathode surges did not provide any sustained voltage recovery, indicating that cathode channel flooding was not a problem under these conditions.

Anode channel nitrogen plugging.— In this section we discuss the portions of the data and delineate the limitations of the purging and surging methodology used for detecting the approximate location of water in the direction perpendicular to the membrane plane.

The first limitation is apparent when the 2D distribution of water along the channels is such that a purge or a surge cannot remove a significant amount of water. At lower current density, 189 mA cm^{-2}, the liquid water was more evenly distributed, rather than concentrated at the end of the channel. Due to the low rate of water generation and subsequently small droplet growth rate, the liquid droplets on the surface of the anode GDL did not grow large enough during the observed time between purges so that they would be pulled by gravity to the end of the channel. It was observed that only liquid water at the end of the anode channel is effectively removed by purging.

This is seen in the buildup of liquid water mass in the anode channel, Fig. 8 between $t = 2200–2275$ min and in Fig. 9 between $t = 3550$ and 3650 min, which is insensitive to anode purges. At higher current densities, there is a greater liquid production and crossover rate; hence, water collects near the end of the anode channels, as shown in Fig. 7c, and repeatable liquid water transients occur.

The second limitation in using the voltage-purge relation for diagnosing anode water plugging arises from the effects of nitrogen crossover and eventual nitrogen accumulation in the anode. In the event of nitrogen flooding, an anode purge can also improve the cell voltage. In the collected data there are cases where the image processing indicates that there is no anode water plugging; however, there is a repeatable voltage improvement after every purge event. Specifically, Fig. 10 ($t = 5400–5480$ min) shows data at higher temperature (60°C) and low cathode inlet RH (40%), where anode channel flooding was no longer detected in the neutron images. For these conditions, the total water content in the GDL decreases sig-
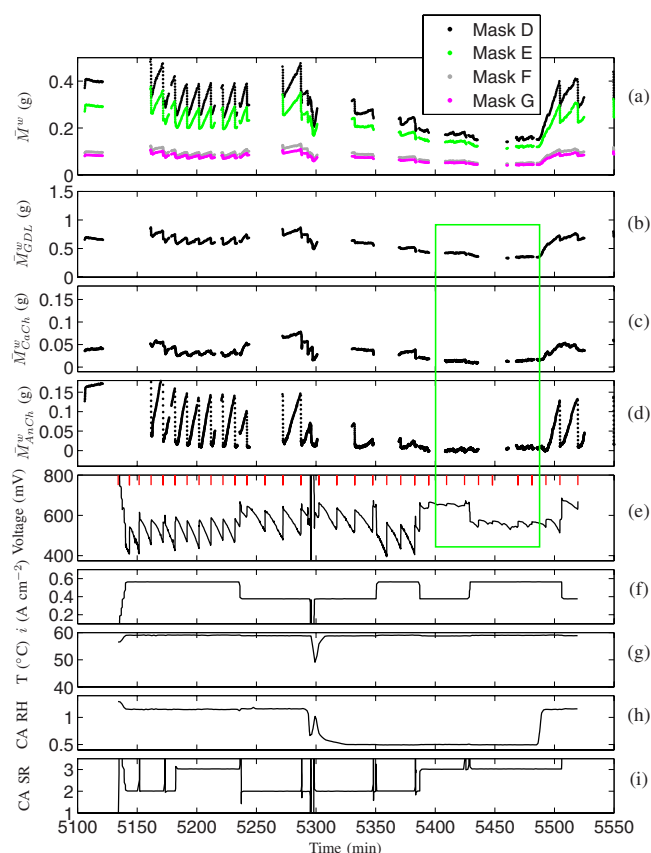
Figure 10. (Color online) Data set 4: Measured total liquid water mass, estimated membrane/GDL and channel liquid water masses, voltage, current density, temperature, CA RH, and CA SR. Both saturated and subsaturated cathode gas (air) conditions with dry hydrogen. At $t = 3800$ min the bubbler is filled with colder water, causing a drop in inlet CA RH. The (red) vertical lines in the voltage subplot indicate anode purges.

nificantly, about half that of the case with a fully humidified cathode inlet, because the water carrying capacity of air increases exponentially with temperature and therefore can remove far more liquid water under these conditions.[16,29] Nonwater anode plugging conditions are also shown in Fig. 8 ($t = 2475$–2530 min) while operating at relatively low current density (377 mA cm^{-2}), high cathode stoichiometric ratio, high temperature, and subsaturated cathode inlet flow.

Nonwater anode plugging conditions were also encountered in the first day of testing shown in Fig. 6 ($t = 700$–780 min) and ($t = 965$–1045 min) where fully saturated air flow was fed to the fuel cell. Some discussion of these two cases is warranted, as the membrane water dynamics and the thermal dynamics[16] might explain why we do not have water anode plugging in these two cases. The period ($t = 700$–780 min) in Fig. 6 was after start-up where the membrane might not have been fully hydrated and hence, might have been absorbing water from the surrounding GDLs. At $t = 925$ min a slow temperature rise of about 5°C was measured at the end plates, following the current density increase to 566 mA cm^{-2}. It is expected that the current increase causes a large spatial gradient in temperature. The thermal history of the membrane impacts the membrane water uptake and conductivity.[30,31] This thermal history may account for the absence of anode flooding following the return to lower current density and nominal temperature at $t = 1000$ min in Fig. 6, conditions which previously ($t = 830$–850 min) exhibited anode channel flooding.

In all the cases where nonwater anode plugging is observed, except the start-up period of Fig. 6 ($t \leq 780$ min), the combined

GDL plus membrane water mass, estimated through masking, was less or equal to 0.5 g, which translates to a volume fraction of liquid water of $s = 0.21$. Because no liquid water is flowing to the anode channel, we assume this value to be equal to the immobile saturation limit s_{im}. A linear GDL compression of 20% is assumed for this calculation, which yields a compressed porosity of $\epsilon = 0.67$, and we assume that the water is distributed evenly between the anode and cathode GDL layers.

Flooding, Plugging, and Voltage Response

A consistent correlation between voltage and anode purging was observed at low-to-medium current density under a variety of operating conditions. This relationship can be used to establish a phenomenological model that connects the accumulation of water and nitrogen in the channel with an apparent active area available for the reaction and hence, establish an easily tunable model with low computational complexity for control applications.[8,9]

The hypothesis of a direct effect of anode channel water and nitrogen mass accumulation on voltage is controversial, as most existing models use the decrease of reactant pressure and the effect of liquid water accumulation in the cathode GDL-catalyst interface on voltage,[32,33] assuming a thin-film model which predicts the blockage of the cathode catalyst interface.[2] A similar argument is used here to formulate an anode channel interfacial blockage which leads to an apparent active area, hence, an apparent current density and consequently, a voltage degradation, as shown in the Appendix.

We first focus on the testing periods where voltage decay is observed but no channel, nor GDL water mass is accumulating. A simple model using published membrane crossover values for nitrogen[19] confirms our hypothesis that nitrogen crosses over from the air supplied cathode through the membrane, accumulates in the anode, and contributes to the measured voltage degradation. The confirmation of the hypothesis is based on the good match between the predicted and the measured voltage degradation between purges. The exact accumulation of nitrogen in the anode channel has to be confirmed with independent nitrogen concentration measurements, which will be the subject of future work.

We then focus on certain periods of testing that show anode flooding and voltage decay and demonstrate that a simple one-dimensional (1D) (channel-to-channel through the membrane), isothermal, and lumped parameter model can be used to predict the transient anode water accumulation and voltage behavior well during anode flooding conditions under dead-ended operation.[8,18,34]

For the model validation we first use test periods with anode flooding without concurrent cathode flooding. Another detailed graph shows a period where anode flooding and voltage decay exhibit a characteristic two-slope behavior, corroborating the hypothesis of voltage decay due to anode plugging instead of cathode catalyst flooding. Finally, a detailed view of a testing period with concurrent anode and cathode flooding is used for the model validation.

Anode nitrogen plugging and voltage response.— Figures 6, 8, and 10 contain boxes which highlight a portion of the experiments where a small voltage degradation, 2 mV min^{-1}, is not correlated to any liquid water accumulation. As one can see, the voltage pattern is repeatable between purges despite the lack of any similar pattern in the water observed. The portions of the experimental data indicate that nitrogen accumulation in the anode channels should be responsible for the relatively small (2 mV min^{-1}) vs the larger (5–8 mV min^{-1}) voltage drop that we typically observe during anode water plugging conditions.

To investigate the effects of nitrogen a channel-to-channel lumped parameter mass balance can be used to calculate the rate of nitrogen accumulation using the permeation coefficient $k_{N_2} = 10^{-14}$ mol m^{-1} s^{-1} Pa^{-1}.[19] At the pressure conditions highlighted in Fig. 6 ($t = 960$–1045 min), a predicted nitrogen accumulation of 0.15 mg min^{-1} in the anode leads to a drop of hydrogen partial pressure of 2 kPa min^{-1}. Assuming homogeneous channel condi-

tions, the reduction in hydrogen partial pressure affects the cell voltage through Eq. A-4 (see the Appendix), and this leads to a voltage drop of only 0.6 mV min^{-1} instead of 2 mV min^{-1} observed here. Because a large change in hydrogen partial pressure alone cannot account for the significant voltage drop observed in the data, we model an effective active area, which represents the nonblocked area that the reactants can easily reach the catalyst sites. Using the effective area, we can calculate the apparent current density, which is caused by displaced hydrogen in the anode channel. Specifically, in a pressure-regulated cell with dead-ended anode, nitrogen will be pushed by the feed gas and accumulate at the end of the channel.[19] So if complete anode channel plugging is assumed to occur when 100% of the anode cross-sectional area has been filled with nitrogen, then the predicted nitrogen accumulation of 0.15 mg min^{-1} will result in a voltage decay of 2.2 mV min^{-1} [using Eq. A-1 and A-2 (see the Appendix)] from A_{app}, by replacing t_* with the channel depth, $m_{*an,ch}$ with the anode channel accumulated nitrogen mass, and ρ_* with nitrogen density. It is most likely that accounting for the diffusion and mixing between hydrogen and nitrogen in the channel using an along-the-channel model will correct for the estimated higher voltage drop. Nevertheless, the simplicity of the model provides a remarkable match with the experimental observations of nitrogen plugging effects on voltage response.

Anode water plugging and voltage response.— A summary of the imaging data indicates that for the majority of the tested conditions anode water plugging should be considered in order to model the cell performance. Nitrogen should clearly also be considered, but the accelerated rate of voltage decay when water plugging is observed requires a more rapid control action and better modeling to prevent potential damage to the cell. A model which includes the effect of both nitrogen and liquid water on voltage requires a more detailed channel model to determine the reduction in active area. Standard diffusion and density values for the hydrogen and nitrogen gases and a simple along-the-channel model, not-yet published, indicate that the anode constituents form stratified layers with liquid water, followed by a nitrogen-rich and then a hydrogen-rich area as we approach the channel inlet. The resulting fuel cell area, which is unavailable to support the reaction, is given by the sum of the nitrogen and water-covered areas. The mass of liquid water accumulated in the anode channel is calculated using well-known equations for the membrane water transport[8,35-37] and the 1D (channel-to-channel, through-membrane plane), isothermal, two-phase (liquid and vapor) flow of water through the GDL. For a detailed description of the water crossover through the membrane, the two-phase flow through the GDL, and the accumulation of liquid in the channel, see Ref. 8.

The neutron imaging data, with the applied masking techniques, confirm the presence of liquid water in the anode channel, as shown in Fig. 11 for a typical purge cycle which was taken from the third day of testing, shown in Fig. 9. The vertical lines shown in the voltage subplot indicate anode purge events. Following an anode purge, all of the liquid water in the anode channel is removed and then slowly accumulates until the next purge event. Note that there is little change in the cathode channel water mass between or during purges.

Following the anode purge, a cathode surge is conducted at approximately 3963 min. During the surge, the cell voltage increases due to the higher oxygen partial pressure. However, after the cathode flow rate is restored, the voltage returns to its previous value. The mass of liquid water in the cathode channel decreases as a result of the increased water removal rate with higher gas flow rate during the surge. In some experiments, even when the cathode surge event occurs just preceding the anode purge event, the voltage continues to degrade at the same rate as experienced before the cathode surge. These results indicate that liquid water in cathode channel has little effect on voltage under these conditions. In contrast, following the two anode purges at 3947 and 3962 min, the voltage recovery is significant and sustained until liquid water begins to accumulate in
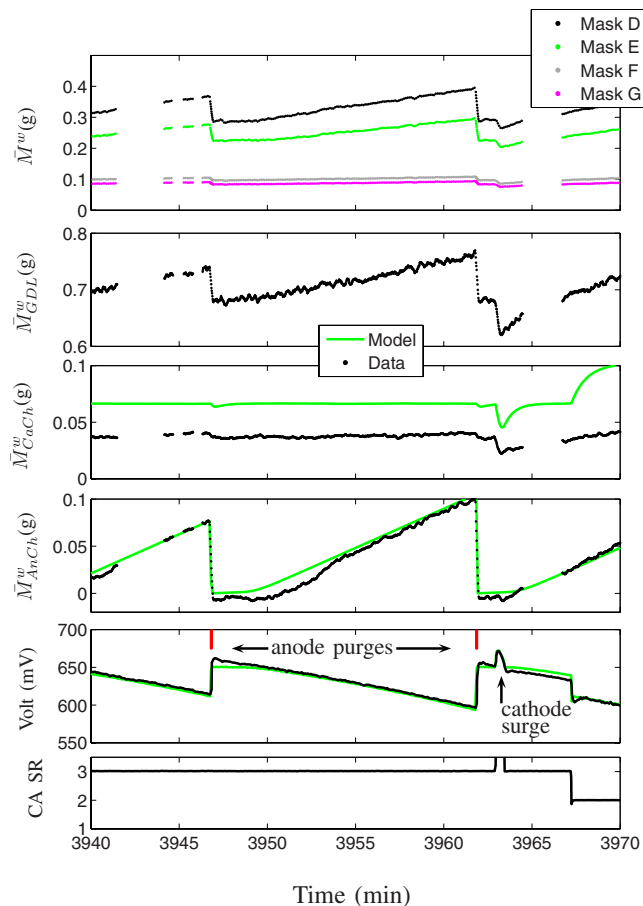

Figure 11. (Color online) Measured cell voltage degradation and liquid water mass accumulation between anode purges, taken from the third data set. These experiments were conducted with fully humidified air at a current density of 378 mA cm^{-2}, a cell operating temperature of 50°C, and an air stoichiometry of 300%.

the anode channel again. There exist other operating conditions, where accumulation of water in the cathode is detected and a sustained voltage recovery occurs following a cathode surge.

Figure 12 shows no liquid water accumulation in the cathode channel, with anode channel water accumulation between purges. Following the anode purge at $t = 2425$ min, the imaging data shows a period with no water accumulation in the channel followed by a linear increase with time. This distinct, two-slope behavior of liquid water accumulation can be explained by a "strong" anode purge which removed liquid water from the GDL. In this case, water accumulation in the channel has two modes, a slow mode which represents vapor transport through the GDL with condensation along the GDL. Once the accumulation of water in the GDL has surpassed the immobile saturation limit,[8,18,38] then both capillary liquid and vapor flow into the channel are present, yielding a faster rate of liquid water accumulation in the channel. Hence, following an anode purge which removes water from the GDL, it takes time before water begins to accumulate in the channel again. The observed voltage degradation under this condition is very well correlated with the two-slope liquid water accumulation in the anode channels and has excellent repeatability. The simulated response using the channel-based apparent current density shows an excellent match despite the two-slope behavior. It would be interesting to investigate whether voltage models that depend on catalyst flooding (water accumulation at the membrane catalyst interface) alone can capture the observed behavior.

Figure 13 shows the voltage during a substantial change in liquid water mass for both the anode and cathode channels. Specifically,
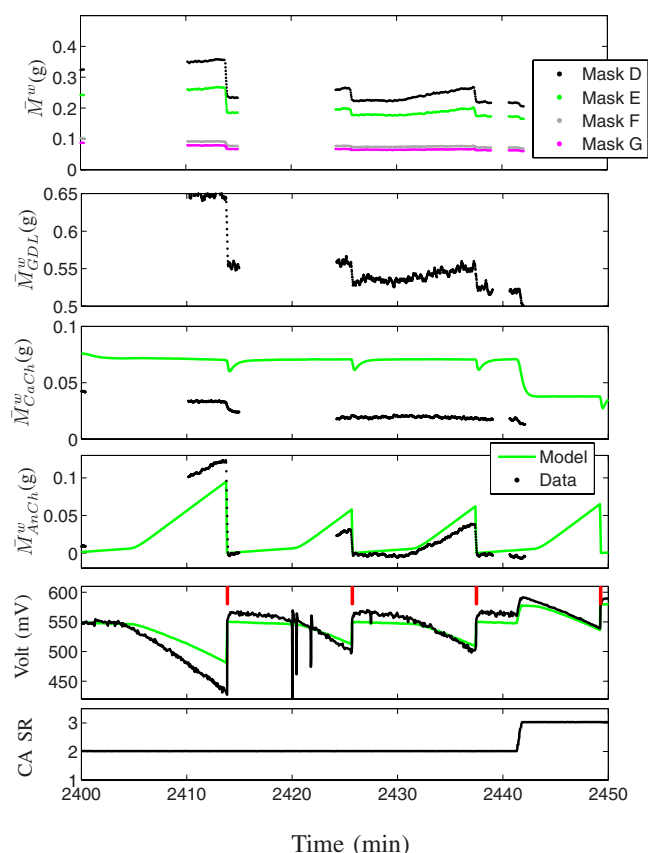
Figure 12. (Color online) Voltage is well correlated with anode liquid water, two-slope behavior at 60°C, 566 mA cm^{-2}, and with a 75% RH for cathode gas stream at 200% stoichiometry.

Figure 13. (Color online) Voltage is well correlated with anode liquid water at 50°C, 377 mA cm^{-2}, and with a 75% RH for cathode gas stream at 200% stoichiometry.

the slow decay in voltage, shown in Fig. 13, can be attributed to the stored anode channel water accumulation. Here the observed voltage clearly depends on both cathode catalyst layer and channel water mass. A cathode surge at $t = 2387$ min removes liquid water from the GDL and cathode channel, resulting in voltage recovery attributed to cathode flooding, which could be caused by blockage of the catalyst or a reduction in oxygen partial pressure due to channel plugging. The simulation results show that the model prediction is reasonable during these testing conditions. Better prediction accuracy could be expected by including the membrane catalyst domain in the modeling approach, yet the model employed here is simple enough to allow real-time predictions, even in automotive microcontroller hardware.[39]

The data analysis and Fig. 8-10 demonstrate that for the majority (80%) of the tested conditions (Table I) the notion of apparent current density, which relates the accumulated mass of liquid water in the anode channel to voltage degradation, can be used to estimate the cell voltage. This estimate agrees well with the measured value, both between purges as well as during purging and surging events when anode water plugging conditions are observed. Fast voltage responses due to the increase in oxygen partial pressure during surges are also estimated well due to the inclusion of the fast reactant dynamics associated with gas concentrations. For the range of current densities tested, a fully humidified cathode gas stream was sufficient to ensure anode flooding conditions, although at higher current density this may not hold.[25] In the case when the cathode inlet gas is fully humidified, the cathode channel always contains a saturated gas stream; therefore, we can assume that there is no vapor pressure gradient along the channel, which implies a uniform boundary condition along the cathode channel and consequently allows us to neglect the variation along the channel and employ a 1D
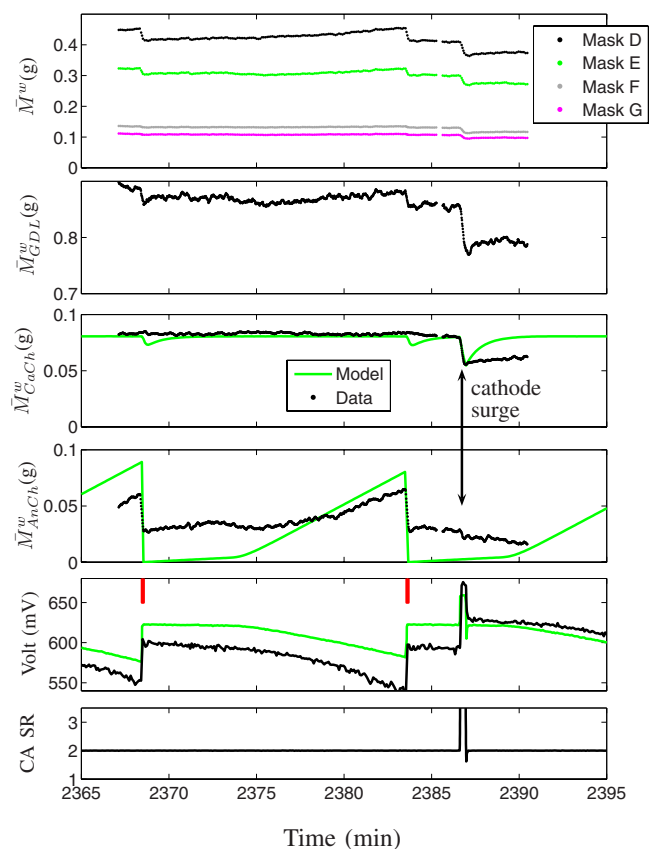
(through-the-membrane) modeling approach for the water dynamics. A similar argument is used in Ref. 40 to show how uniform boundary conditions in a 2D fuel cell model can be treated as a 1D partial differential equation system. The model currently is not able to predict anode drying conditions when the cathode inlet RH < 80%, because the assumption of uniform channel conditions in the lumped model may be violated. When a subsaturated gas stream is supplied to the cathode, there will be a gradient in vapor concentration along the cathode channel, leading to a time-varying and spatially varying boundary condition along the cathode channel. As current density and air flow rate change, the point along the channel at which the gas stream becomes fully saturated will move,[16] which effects the net membrane water transport.

Conclusion

The mass of liquid water in an operating single-cell fuel cell was measured at the NIST neutron imaging facility under dead-ended anode operation. Image masks, based on the cell design, were employed to calculate liquid water mass in the anode vs cathode gas channels and the combined membrane and anode–cathode GDLs. Anode purges and cathode surges were conducted to remove liquid water, correlate the water removal to voltage improvement, and visually confirm the approximate location of the accumulated liquid water inside the fuel cell. The observed voltage recovery during these purges and surges can be employed as a diagnostic tool indicating anode or cathode plugging and flooding.

Anode channel water plugging followed by a significant (5–8 mV min^{-1}) voltage decrease was observed even without cathode channel water plugging, indicating the importance of anode flooding to cell performance. This points to the need for further understanding the fuel cell performance limitations associated with anode operating conditions.

The observed voltage and liquid water accumulation in the anode channel exhibit a distinct and repeatable two-slope transient behavior after an anode purge. This points to a direct phenomenological relationship between the water mass accumulated in the anode channel and the cell voltage. We employ such a relation using the notion of apparent current density and show that a simple 1D (through the membrane) model can capture the observed dynamic fuel cell behavior under a wide range of operating conditions.

Future work is underway to collect data with different GDL, membrane material, and cell orientation with different temperature and current densities to verify the observed patterns. Additionally, experiments with concurrent measurement of nitrogen concentration in the anode gas channels will be pursued.

Appendix
Voltage Model

In our model, the resulting voltage degradation is related to the accumulation of liquid water mass in the anode channel, $m_{l,an,ch}$, which is assumed to form a thin film of thickness, t_{wl}, blocking part of the active fuel cell area, A_{fc}, to give an effective active area, A_{app}, in m^2

$$A_{app} = A_{fc} - \frac{1.3 m_{*,an,ch}}{n_{cells}\rho_* t_*} \qquad [A-1]$$

The scaling factor of 1.3 is the ratio of the total active area to the anode channel area, since only that surface area at the channel interface can be covered with liquid. In the case of water plugging the thickness of the water layer, t_{wl} is a tunable parameter that impacts the rate of voltage decay as liquid water accumulates. A similar notion of reduced area is used in Ref. 41 to account for the reduction in fuel cell output power when the anode is filled with liquid water. In the case when nitrogen plugging is considered, Eq. A-1 can also be used to calculate the effective area, but the actual channel depth is used instead for t_* instead of a tunable parameter. Using the apparent area, an apparent current density, i_{app} in A/cm^2, can be calculated

$$i_{app} = \frac{I_{st}}{10000 A_{app}} \qquad [A-2]$$

where I_{st} is the current drawn from the cell in amperes and the apparent fuel cell area.

The cell voltage, v, is parameterized using a mechanistic voltage model[34,42] with apparent current density and membrane resistance,[35]

$$v = E - U_{act} - U_{ohmic} \qquad [A-3]$$

where E is the theoretical open-circuit voltage, given by

$$E = -\left(\frac{\Delta H}{2F} - \frac{T\Delta S}{2F}\right) + \frac{RT}{2F}\ln\left(\frac{p_{H_2,an,mb}\sqrt{p_{O_2,ca,mb}}}{(p_o)^{1.5}}\right) \qquad [A-4]$$

with ΔS and ΔH being the differences in entropy and enthalpy from standard state conditions, p_o is the standard pressure, and $p_{O_2,ca,mb}$ and $p_{H_2,an,mb}$ are the oxygen and hydrogen partial pressures at the GDL–membrane interface. The activation voltage loss, U_{act},[34] is given by

$$U_{act} = K_1 \frac{RT}{F}\ln\left(\frac{i_{app}}{i_o}\right) \qquad [A-5]$$

which includes the apparent current density and the exchange current density, i_o

$$i_o = K_2\left(\frac{p_{O_2,ca,mb}}{p_o}\right)^{K_3}\exp\left[-\frac{E_c}{RT}\left(1 - \frac{T}{T_o}\right)\right] \qquad [A-6]$$

where E_c is the activation energy for oxygen reduction on Pt, and T_o is the reference temperature.

Finally, the ohmic voltage loss, U_{ohmic}, is taken from[35]

$$U_{ohmic} = K_4\left[\frac{t_{mb}}{(b_{11}\lambda_{mb} - b_{12})}e^{-1268[(1/303)-(1/T)]}\right]i_{app} \qquad [A-7]$$

where t_{mb} is the membrane thickness, λ_{mb} is the membrane water content, and b_{11} and b_{12} are experimentally identified parameters.

The values for $m_{l,an,ch}$, $p_{O_2,ca,mb}$, and $p_{H_2,an,mb}$ are calculated based on a simple 1D (channel-to-channel through the membrane), isothermal, and lumped parameter model.[8] The parameters K_1–K_4 are tuned using a least-squares method on data from all testing conditions shown in Fig. 6 and 8-10. The water film thickness, t_{wl}, is tuned by comparing the rate of voltage decay using the measured cell impedance ($R = 4.3$ mΩ) to the measured cell voltage for selected purge cycles taken from the 4 days of testing. If the voltage degradation is all attributed to liquid water, we find that a water thickness of $t_w = 0.12$ mm is required to achieve the matching voltage degradation as calculated from $v = i_{app}A_{fc}R$.

References

1. R. J. Bellows, M. Y. Lin, M. Arif, A. K. Thompson, and D. Jacobson, *J. Electrochem. Soc.*, **146**, 1099 (1999).
2. P. A. Chuang, A. Turhan, A. K. Heller, J. S. Brenizer, T. A. Trabold, and M. M. Mench, in *The Third International Conference on Fuel Cell Science, Engineering and Technology*, p. 31 (2005).
3. Y.-S. Chen, H. Peng, D. S. Hussey, D. L. Jacobson, D. T. Tran, T. Abdel-Baset, and M. Biernacki, *J. Power Sources*, **170**, 376 (2007).
4. J. St-Pierre, D. P. Wilkinson, S. Knights, and M. Bos, *J. New Mater. Electrochem. Syst.*, **3**, 99 (2000).
5. J. P. Meyers and R. M. Darling, *J. Electrochem. Soc.*, **153**, A1432 (2006).
6. M. Arcak, H. Gorgun, L. Pedersen, and S. Varigonda, *IEEE Trans. Control Syst. Technol.*, **12**, 101 (2004).
7. J. Pukrushpan, A. Stefanopoulou, S. Varigonda, L. Pedersen, S. Ghosh, and H. Peng, *IEEE Trans. Control Syst. Technol.*, **13**, 3 (2005).
8. D. A. McKay, J. B. Siegel, W. Ott, and A. G. Stefanopoulou, *J. Power Sources*, **178**, 207 (2008).
9. J. B. Siegel, D. A. McKay, and A. G. Stefanopoulou, in *2008 American Control Conference*, p. 2573 (2008).
10. H. Ju, G. Luo, and C.-Y. Wang, *J. Electrochem. Soc.*, **154**, B218 (2007).
11. D. Kramer, J. Zhang, R. Shimoi, E. Lehmann, A. Wokaun, K. Shinohara, and G. Scherer, *Electrochim. Acta*, **50**, 2603 (2005).
12. T. Trabold, J. Owejan, D. Jacobsen, M. Arif, and P. Huffman, *Int. J. Heat Mass Transfer*, **49**, 4712 (2006).
13. R. Satija, D. L. Jacobson, M. Arif, and S. A. Werner, *J. Power Sources*, **129**, 238 (2004).
14. A. Turhan, K. Heller, J. Brenizer, and M. Mench, *J. Power Sources*, **160**, 1195 (2006).
15. K. Yoshizawa, K. Ikezoe, Y. Tasaki, D. Kramer, E. H. Lehmann, and G. G. Scherer, *J. Electrochem. Soc.*, **155**, B223 (2008).
16. M. A. Hickner, N. P. Siegel, K. S. Chen, D. S. Hussey, D. L. Jacobson, and M. Arif, *J. Electrochem. Soc.*, **155**, B294 (2008).
17. D. Hussey, D. Jacobson, and M. Arif, in *Proceedings of the ASME International Conference on Fuel Cell Science, Engineering and Technology*, Fuel Cell 2007-25125, p. 31 (2007).
18. D. A. McKay, W. T. Ott, and A. Stefanopoulou, in *Proceedings of 2005 ASME International Mechanical Engineering Congress & Exposition*, Vol. IMECE 2005-81484 (2005).
19. S. S. Kocha, J. D. Yang, and J. S. Yi, *AIChE J.*, **52**, 1916 (2006).
20. R. Ahluwalia and X. Wang, *J. Power Sources*, **171**, 63 (2007).
21. D. Natarajan and T. Van Nguyen, *J. Electrochem. Soc.*, **148**, A1324 (2001).
22. M. Hickner, N. Siegel, K. Chen, D. McBrayer, D. Hussey, D. Jacobson, and M. Arif, *J. Electrochem. Soc.*, **153**, A902 (2006).
23. R. Hassanein, E. Lehmann, and P. Vontobel, *Nucl. Instrum. Methods Phys. Res. A*, **542**, 353 (2005).
24. B. A. McCain, A. G. Stefanopoulou, and I. V. Kolmanovsky, in *46th IEEE Conference on Decision and Control*, IEEE, pp. 584–589 (2007).
25. A. Y. Karnik, A. G. Stefanopoulou, and J. Sun, *J. Power Sources*, **164**, 590 (2007).
26. N. Pekula, K. Heller, P. Chuang, A. Turhan, M. Mench, J. Brenizer, and K. Unlu, *Nucl. Instrum. Methods Phys. Res. A*, **542**, 134 (2005).
27. E. Kimball, T. Whitaker, Y. G. Kevrekidis, and J. B. Benziger, *AIChE J.*, **54**, 1313 (2008).
28. Z. H. Wang, C. Y. Wang, and K. S. Chen, *J. Power Sources*, **94**, 40 (2001).
29. A. Turhan, K. Heller, J. Brenizer, and M. Mench, *J. Power Sources*, **180**, 773 (2008).
30. L. Onishi, J. Prausnitz, and J. Newman, *J. Phys. Chem. B*, **111**, 10166 (2007).
31. A. Weber and J. Newman, *Chem. Rev. (Washington, D.C.)*, **104**, 4679 (2004).
32. P. Berg, K. Promislow, J. S. Pierre, J. Stumper, and B. Wetton, *J. Electrochem. Soc.*, **151**, A341 (2004).
33. G. Lin, W. He, and T. V. Nguyen, *J. Electrochem. Soc.*, **151**, A1999 (2004).
34. F. Barbir, *PEM Fuel Cells: Theory and Practice*, Elsevier, Burlington, MA (2005).
35. T. Springer, T. Zawodzinski, and S. Gottesfeld, *J. Electrochem. Soc.*, **138**, 2334 (1991).
36. J. Hinatsu, M. Mizuhata, and H. Takenaka, *J. Electrochem. Soc.*, **141**, 1493 (1994).
37. K. Dannenberg, P. Ekdunge, and G. Lindbergh, *J. Appl. Electrochem.*, **30**, 1377 (2000).
38. J. Nam and M. Kaviany, *Int. J. Heat Mass Transfer*, **46**, 4595 (2003).
39. B. A. McCain, J. B. Siegel, and A. G. Stefanopoulou, in *American Control Conference*, p. 5098 (2008).
40. A. Z. Weber, R. M. Darling, and J. Newman, *J. Electrochem. Soc.*, **151**, A1715 (2004).
41. C. H. Woo and J. Benziger, *Chem. Eng. Sci.*, **62**, 957 (2007).
42. D. Cheddie and N. Munroe, *J. Power Sources*, **147**, 72 (2005).